Higher-order continuation method for the rigid-body kinematic design of compliant mechanisms

Lennart Rubbert, Isabelle Charpentier, Simon Henein, Pierre Renaud

Higher-order continuation method for the rigid-body kinematic design of compliant mechanisms

Lennart Rubbert[1a,b], Isabelle Charpentier[a], Simon Henein[b], Pierre Renaud[a]

[a]*AVR - ICube, CNRS - Université de Strasbourg - INSA Strasbourg, 300 bd Sébastien Brant, F-67412 Illkirch, France*
[b]*Instant-Lab, EPFL-STI-IMT, rue de la Maladière 71b, CH-2000 Neuchâtel, Suisse*

Abstract

Compliant mechanisms are of great interest in precision engineering. In this paper we propose a higher-order continuation method to help their rigid-body kinematic design. Higher-order continuation method leads to direct accurate plotting of the input-output relationship of any mechanism using only its geometrical closed-loop equations, i.e. without complex derivation of any analytical model. These plots, called bifurcation diagrams, reveal essential information as joint velocity profile and the presence of singular configurations. Moreover, the continuous and accurate computation of the mechanism configuration in the vicinity of singularities provides detailed information about the kinematic behavior of the mechanism in its extreme positions. For the design of compliant mechanisms, the designer can advantageously use the bifurcation diagrams to first evaluate the relevance of the selected mechanism, then identify a working configuration in order to obtain adequate kinematic properties without the derivation of the inverse kinematic model (IKM) or the direct kinematic model (DKM). The method is exemplified with a 3 universal-joint and 3 spherical-joint mechanism (3–US) mechanism, the IKM and DKM of which cannot be derived analytically. The latter has a large workspace and special kinematic behaviors consisting of a screw-like motion and platform gyration, which have not been studied before and could lead to interesting novel devices.

Keywords: compliant mechanism, mechanical design, continuation method, bifurcation diagram, 3–US mechanism, singularity, workspace analysis

1. Introduction

The advantages of compliant mechanisms for precision applications are well known [2]. Their design can be efficiently performed using the so-called rigid body replacement (RBR) method [1]. The synthesis is then achieved by relying on a rigid-body mechanism, taking into account the properties of compliant joints by spring models. Given their stiffness properties, parallel mechanisms are in this context of particular interest for the development of compliant structures. Several studies are focused on the selection of appropriate parallel architectures for the design of compliant mechanisms [4, 3, 14], which is a difficult design issue for two reasons. Firstly, a great number of parallel mechanisms exist, including solutions with less than six degrees-of-freedom (DOF) that have the advantage of simple mechanical design [7] and large workspace [8]. During the synthesis of a compliant mechanism using the RBR method, one difficulty is to select an adequate parallel mechanism, which requires comparing numerous designs. Secondly, compliant mechanisms usually have a limited workspace, and their synthesis therefore consists in determining the most adequate configuration in the rigid-body mechanism workspace. The determination of a relevant mechanism configuration is therefore also an issue, since parallel mechanisms can have a complex workspace, and kinematic properties can largely vary within that workspace with presence of kinematic singularities. Efficient kinematic analysis with determination of the presence of singularities is needed.

Several studies have been focused on the determination of mechanism workspace. Monte Carlo method [15], branch-and-prune algorithm [16] as well as geometrical approaches [17, 18] have been proposed. These methods exploit *a priori* knowledge of the mechanism properties to reduce computation time, which constitutes a serious

[1]Corresponding author, lennart.rubbert@insa-strasbourg.fr, Phone: + 33 3 88 14 47 00

drawback during a mechanism synthesis when several designs have to be compared. It has been demonstrated that the workspace boundaries corresponds to singularity locii [19]. Haug *et al.* [20] and recently Hentz *et al.* [21, 22] have consequently developed continuation-based methods to determine the workspace outer envelope by following one-dimension paths on it. Any mechanism can be analyzed after simply deriving the geometrical closed-loop equations, and with a limited computation time. This constitutes very interesting features for a systematic evaluation of mechanism, but no information is obtained on accessible configurations within the workspace. In this paper, we introduce an evaluation method based on the same theoretical background but with a complementary approach giving information on the boundary and the inner properties of the workspace.

Kinematic analysis to study the geometrical model and properties of robots have been developed using different methods including analytical [10, 9] and geometrical approaches [11, 8]. Both have their limitations since obtaining an analytical model is not always possible and the geometrical approach efficiency strongly depends on the mechanism and the user expertise. Moreover, considering the analysis of robot singular configurations, analytical approaches generally fail. For these particular situations, Grassman-Cayley algebra and screw theory can be used to prove the existence of singularity and to identify the nature of singular movements [14]. However, these methods lack generality and require advanced knowledge on the mechanism as well as designer expertise to determine the mechanism kinematic properties. This is an issue, since singularities are either explicitly avoided or used for the synthesis of compliant structures as detailed in [12].

A first main contribution of the present paper is a method identifying the presence of singularities for a mechanism along any given set of end-effector configurations, at no extra computation time and with no loss of generality. A second main contribution is the ability that offers the method to determine workspace and kinematic properties of mechanisms that can be employed using only basic knowledge of a mechanism. It builds on the higher-order continuation method [23, 24] for the continuous computation of joint angular positions along any parameterized end-effector path. The results are presented in the form of so-called bifurcation diagrams displaying joint positions as functions of the end-effector position. A third main contribution is that precise information on the mechanism kinematic properties can be extracted, helping the designer in choosing a mechanism, its configuration, the actuated joints or the joints to be suppressed in the particular situations of singularities.

The method is exemplified by a study of the kinematic behavior of the 3–US mechanism. Composed of three identical legs connected to the end-effector (Fig.1), this mechanism is of simple architecture and can be of great interest for compliant mechanisms. Each leg is linked to the base with a universal joint (U) and to the end-effector with a spherical joint (S). The mechanism is also interesting because of the motions it can exhibit when the end-effector lies in the plane of the base (Fig.1, left). As outlined in [12, 13, 14], the end-effector then exhibits two rotations around axes in the base plane and a translation in the direction perpendicular to the plane. Such motions have been successfully used in the surgical context for a compliant device [14]. Beyond this use, very little information exists on the properties of the mechanism. It is therefore a case study that is suited for the introduction of the proposed approach.

The paper is structured as follows: the 3–US kinematic modeling is introduced in Section 2 to outline the available information on the mechanism. This sets the general formulation used in the method. The higher-order continuation method is introduced in Section 3: it is the core of the general analysis. We propose to use the Diamanlab software [25] and describe its main underlying principles. The analysis of the mechanism properties, including the workspace boundaries and interesting features such as screw motion and self-motion are discussed in Section 4. A summary and an outlook are proposed in Section 5.

2. Case study description: the 3–US mechanism

2.1. Introduction and parameterization

We consider the parameterization of the 3–US mechanism as given in Fig. 2. It is designed with three identical legs equally distributed along a circle of radius R and center O. Each leg i, $i \in \{1, 2, 3\}$, is composed of a universal

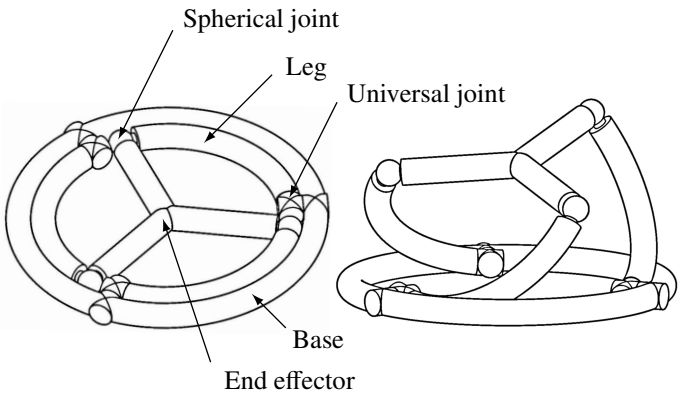

Figure 1: In-plane (left) and out-of-plane (right) configurations of the 3–US mechanism.

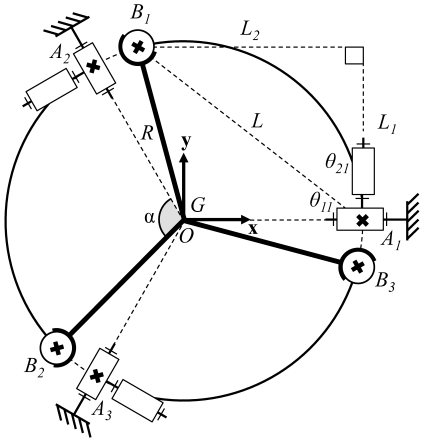

Figure 2: Parameterization of the 3–US mechanism.

joint rigidly connected to a spherical joint. The universal joint center A_i is located at the intersection of the axes of its two revolute joints. The axes of the first revolute joint of the universal joints intersect at O. The base frame is chosen with O as center, vector $\mathbf{x}$ aligned with $\mathbf{OA_1}$ and vector $\mathbf{y}$ in the base plane. For symmetry reasons, the points A_i are positioned with angles $\angle A_1OA_2 = \angle A_2OA_3 = \angle A_3OA_1 = 2\pi/3$. This joint arrangement is of particular interest as it allows for the deployment of the structure [13]. The single plane containing O and the points A_i is designated as the base plane in the following.

The center of the spherical joint of leg i is denoted by B_i. The centroid of the triangular platform $B_1B_2B_3$ is denoted by G. The configuration of the spherical joint centers is such that $GB_i = OA_i$, $i \in \{1, 2, 3\}$, so that the mechanism architecture is defined only by two geometrical parameters: the radius $R = OA_i = GB_i$ and the angle $\alpha = \angle A_iOB_i$, $i \in \{1, 2, 3\}$.

The angular positions of the first and second revolute joints of the universal joints are respectively defined by θ_{1i} and θ_{2i}, $i \in \{1, 2, 3\}$. In the planar configuration depicted in Fig. 2, the angular positions are defined such that $\theta_{1i} = 0$ and $\theta_{2i} = 0$, $i \in \{1, 2, 3\}$. From a technological point of view, actuating the spherical joints is difficult. As the 3–US mechanism has three DOF, we consider that either the first or the second revolute joints are actuated. Both situations and their consequences are numerically studied in section 4. The input and intermediate coordinates are consolidated in the state vector designated by $\mathbf{u} = (\theta_{11}, \theta_{21}, \theta_{12}, \theta_{22}, \theta_{13}, \theta_{23})$.

The platform motions are rotational and translational in most of the cases [14]. Since the mechanism has three DOF, one single set of three variables among the input and output coordinates is sufficient to constrain the mechanism. The coordinates of the platform centroid G is chosen as output coordinate set in order to define the mechanism's configuration and is denoted by $\mathbf{X}$.

2.2. Kinematic model

By definition, the output coordinate set $\mathbf{X}$ satisfies:

$$\mathbf{X} = \mathbf{OG} = \frac{1}{3}\sum_{i=1}^{3} \mathbf{OB_i}, \tag{1}$$

and can be related to the input and intermediate coordinates by expressing the vectors $\mathbf{OB_i}$, $i \in \{1, 2, 3\}$, as:

$$\mathbf{OB_i} = \begin{pmatrix} (R - L_2\cos(\theta_{2i}))\cos\left(\frac{2\pi}{3}(i-1)\right) - (L_1\cos(\theta_{1i}) - L_2\sin(\theta_{2i})\sin(\theta_{1i}))\sin\left(\frac{2\pi}{3}(i-1)\right) \\ (L_1\cos(\theta_{1i}) - L_2\sin(\theta_{2i})\sin(\theta_{1i}))\cos\left(\frac{2\pi}{3}(i-1)\right) + (R - L_2\cos(\theta_{2i}))\sin\left(\frac{2\pi}{3}(i-1)\right) \\ L_1\sin(\theta_{1i}) + L_2\sin(\theta_{2i})\cos(\theta_{1i}) \end{pmatrix}, \tag{2}$$

where $L_1 = R\sin(\alpha)$, $L_2 = 2R\sin(\alpha/2)$[2]. Combining equations (1) and (2) yields three constraint equations linking the output coordinates $\mathbf{X}$ to the state vector $\mathbf{u}$.

Besides, the mobile platform rigidly connects the points B_i, that is:

$$\|\mathbf{B_1B_2}\| = \|\mathbf{B_2B_3}\| = \|\mathbf{B_1B_3}\| = \sqrt{3}R. \tag{3}$$

Expanding equation (3) using the vectors expressions from equations (2) gives three additional constraint equations. The resulting system of six constraint equations for six unknowns is written explicitly in the code presented in Appendix A.

The Inverse Kinematic Model (IKM) and the Direct Kinematic Model (DKM) are generally derived from constraint equations to determine the input-output relation of a mechanism, *i.e.* the geometrical relation between the end-effector and the actuator positions. Specifically the IKM allows computing the actuated joint coordinates for given output coordinates $\mathbf{X}$. Reciprocally, the DKM allows computing $\mathbf{X}$ from the knowledge of the actuated joint coordinates. Even if the mathematical formulation of the constraint equations seems affordable, to the best of our knowledge, the derivation of the IKM or DKM for this mechanism is not achievable in an analytical manner in the general case. Their numerical computation could be considered with for instance a classical Newton-Raphson method, but such use remains difficult in the vicinity of singular configurations. This constitutes a strong limitation since the vicinity of singular configurations is particularly interesting for the design of compliant mechanisms: indeed it corresponds to particular kinematic behavior which can be used notably for motion amplification purpose for example [6, 14]. As outlined in the following, the proposed higher-order continuation method is particularly relevant and accurate in such situations.

3. Mechanism analysis using higher-order continuation method

The workspace exploration of a mechanism can be performed along parameterized paths. For instance, one of the three output coordinates related to the end-effector centroid may be considered as a varying parameter, hereafter denoted λ, while the other two are kept constant.

One deduces from the constraint equations (2) and (3) that the mechanism analysis can be formulated as the general nonlinear parametric problem linking the input and intermediate coordinates $\mathbf{u} \in \mathbb{R}^n$ ($n = 6$ here)

$$\mathcal{R}(\mathbf{u}, \lambda) = 0, \tag{4}$$

where the parameter $\lambda \in \boldsymbol{R}$ is to be varied along the path and $\mathcal{R}$ is a the vector-valued function. The solutions for the under-determined system (4) define one-dimensional continua, hereafter called branches of solutions.

Continuation methods and related software, see [26, 24] enable to compute solution branches. Most of them rely on first order predictor-corrector principles described in [27, 28, 29, 30] and approximate the solution branches as a collection of points satisfying (4). Under analyticity assumptions, continuous solution branches may be actually computed [38, 24].

3.1. Higher-order continuation method

Under analyticity assumptions, the solution for nonlinear problems may indeed be carried out through a Taylor-based numerical method and higher-order Automatic Differentiation (AD) [31, 32, 33, 34]. In a nutshell, AD is a set of techniques that enable to augment a given computer code with derivative computations, with an obvious advantage in terms of ease of implementation and generality since derivative computations, Jacobians and higher-order terms are performed in an automatic manner [24, 35, 36].

The Diamant approach [23, 24] is a higher-order continuation method that automates the Asymptotic Numerical Method discussed in [37, 38]. Diamant is of particular interest for mechanism analysis since it may be used from the constraint equations only. The related Matlab software is named Diamanlab [25, 42].

Following [38, 24], the solution for (4) is performed considering the nonlinear problem:

$$\mathcal{R}(\mathbf{u}(a), \lambda(a)) = 0, \tag{5}$$

$$a = \left\langle \mathbf{u}\,(a) - \mathbf{u}(0), \frac{\partial \mathbf{u}}{\partial a}\,(0) \right\rangle + (\lambda(a) - \lambda(0))\frac{\partial \lambda}{\partial a}\,(0)\,, \tag{6}$$

where a is a measure of the pseudo arc-length (equation (6)) [27] along the branch of solutions $(\mathbf{u}(a), \lambda(a))$ issued from the point $(\mathbf{u}(0), \lambda(0))$. This branch is locally approximated by means of two Taylor series:

$$(\mathbf{u}(a), \lambda(a)) = \Big(\sum_{k=0}^{K} \frac{a^k}{k!} \frac{\partial^k \mathbf{u}}{\partial a^k}(0), \sum_{k=0}^{K} \frac{a^k}{k!} \frac{\partial^k \lambda}{\partial a^k}(0) \Big) = \Big(\sum_{k=0}^{K} a^k \mathbf{u}_k, \sum_{k=0}^{K} a^k \lambda_k \Big), \tag{7}$$

where $\mathbf{u}_k$ and λ_k are the Taylor coefficients of $\mathbf{u}(0)$ and $\lambda(0)$ at order k, and K is the truncation order. Thanks to analyticity, the generic problem (5) written in terms of the Taylor coefficients $\mathcal{R}_k$ of $\mathcal{R}$

$$\mathcal{R}(\mathbf{u}(a), \lambda(a)) = \sum_{k=0}^{K} a^k \mathcal{R}_k = 0, \tag{8}$$

allows to deduce that:

$$\mathcal{R}_k = 0, \quad \text{for } k = 1 \text{ to } K. \tag{9}$$

The Taylor coefficient $\mathcal{R}_k$ ($k = 1, .., K$) may be split into [39]

$$\mathcal{R}_k = \{\mathcal{R}_1\}(\mathbf{u}_k, \lambda_k)^T + \{\mathcal{R}_{k|\mathbf{u}_k=0,\lambda_k=0}\} = 0, \tag{10}$$

where the Jacobian $\{\mathcal{R}_1\}$ of $\mathcal{R}$ is the same over the orders. The higher-order term $\{\mathcal{R}_{k|\mathbf{u}_k=0,\lambda_k=0}\}$ contains the nonlinear contributions that are independent from the unknowns $\mathbf{u}_k$ and λ_k. The higher-order terms and the solutions of linear system (11) are computed each in turn following:

$$\begin{cases} \{\mathcal{R}_{1|\mathbf{u}_1=Id,\lambda_1=1}\}(\mathbf{u}_k, \lambda_k)^T = -\{\mathcal{R}_{k|\mathbf{u}_k=0,\lambda_k=0}\}, & \text{for } k = 1 \text{ to } K, \\ a = (\mathbf{u}_k - \mathbf{u}_0)\mathbf{u}_1 + (\lambda_k - \lambda_0)\lambda_1. \end{cases} \tag{11}$$

Once the series are computed, the *a posteriori* error estimate (12) provides an adaptive step size control based on a numerical radius of convergence a^* of the series [38]

$$a^* = \left(\varepsilon \frac{\|U_1\|}{\|U_K\|}\right)^{\frac{1}{K-1}}, \tag{12}$$

where ε is a small parameter usually chosen equal to 10^{-6}. It also enables to evaluate the interest for a correction. Truncated Taylor series allow for the construction of accurate continuous solution branches and contain information for the detection of bifurcation and instability points [40].

Bifurcation diagrams plot continuous solution branches comprising possible bifurcation points. These bifurcation points correspond to the intersection of branches of solutions. They may be detected either by monitoring a change of sign for the Jacobian determinant along the solution branch [27] or by implementing higher-order bifurcation indicators [40, 41] from Taylor series information. For the sake of generality, see subsection 3.2, Diamanlab (Matlab implementation of Diamant [25, 42]) implements the detection and branch switching processes proposed in [40].

Key points for the automation of the solution (5) are the generality of both the high-level nonlinear solver (11) and AD for Taylor coefficient computations. In other words, only the constraint equations are necessary for the mechanism analysis.

3.2. Implementation with Diamanlab

Diamanlab [42] builds on the general high-level nonlinear solver (11) for the continuous solution of the general nonlinear problem (5). It is therefore of particular interest for mechanism analysis near to singular configurations.

From a user point of view, a nonlinear problem satisfying the analyticity assumption and written as in (5) may be solved by deriving a user class from the general system class of Diamanlab and by implementing the mechanism equations (1)-(2) and (3) as a user method $\mathcal{R}$. Additional user-defined graphics may be coded within the user class. In the following, each exploration is performed with a truncation order of $K = 20$, an threshold of $\varepsilon = 1.10^{-6}$ in (12) and a Newton-Raphson threshold of 1.10^{-6}. Diamanlab moreover provides the detection of bifurcations [40], exploited here to detect the mechanism singularities. A graphical user interface allows for an interactive management of the continuation.

Diamanlab is available for academic research. The software includes a benchmark [25] of classical nonlinear problems as a basis for the implementation of user-defined problems as well as the 3–US mechanism problem. The interested readers may contact the second author for a copy of the Diamanlab software including the 3-US example, see Appendix A.

4. Analysis of the 3–US mechanism properties for compliant mechanism design

The benefits for the design of compliant mechanisms coming from the use of bifurcation diagrams are illustrated considering two meaningful singular situations. The screw motion of the platform obtained when its centroid is displaced along the axis $(O, \mathbf{z})$ is first presented in subsection 4.2 to emphasize the ability of the proposed method to detect parallel and serial singularities. The kinematic behavior is similar to the one exhibited by the Wren mechanism [45, 46]. Second a self-motion due to architectural singularity, with a circular trajectory which has not been presented in the literature before, is described in subsection 4.3. Finally, in subsection 4.4 the workspace boundary is obtained from the bifurcation plots local and global extremum and displayed.

4.1. Preliminary observations

The radius R and the arc length α of the legs are the two geometrical parameters that define the mechanism behavior. The radius R only affects linearly the size of the workspace. It is therefore arbitrarily set to $R = 10$. The angle α influences the volume and the shape of the workspace as well as the kinematic behavior. The angle α is chosen equal to $\frac{\pi}{2}$ in order to avoid leg overlapping, which would strongly reduce the practical interest of the mechanism.

Cylindrical coordinates are adopted with O as origin and $(O, \mathbf{z})$ as axis in accordance with the architecture of the mechanism. The position of the centroid G is denoted by (ρ_G, ϕ_G, z_G) with ρ_G the radius, ϕ_G the angular position and z_G the height. Taking into account the symmetry of the mechanism with respect to the $(O, \mathbf{x}, \mathbf{y})$ plane, the bifurcation diagrams are plotted for $z_G \geq 0$ only.

4.2. Screw motion, bifurcation and kinematic singularities

The proposed analysis is based on the information that can be extracted from bifurcation diagrams. These diagrams are representations of the variable set $\mathbf{u}(\lambda)$ that plot the continuous evolution of $\mathbf{u}$ along the variation of λ. The initial point $(\mathbf{u}(0), \lambda(0))$ is computed from an initial guess using a Newton-Raphson algorithm. Then the continuation takes place and the solution branches of the nonlinear problem under study are computed as sets of Taylor-based solution branches stored in checkpoints [43, 44]. These checkpoints contain information about the initial point $(\mathbf{u}(0), \lambda(0))$, the series and its range of validity, and one (or several) oriented tangent vector that indicates the continuation direction. A branch of solutions is constituted by the evolution of the septuplet $(\mathbf{u}, \lambda) = (\theta_{11}, \theta_{21}, \theta_{12}, \theta_{22}, \theta_{13}, \theta_{23}, \lambda)$. A projected bifurcation diagram is a 2D representation of one or several branches of solutions.

The bifurcation diagram presented in Fig.3a plots the branches of solutions when the position of G varies along the axis $(O, \mathbf{z})$. The end-effector motion path is set by $(\rho_G, \phi_G, z_G) = (0, 0, \lambda)$. For the sake of readability, curves for $(\theta_{12}, \theta_{22})$ and respectively $(\theta_{13}, \theta_{23})$, are shifted by 2π and 4π. From Fig. 3a, it is possible to compute the configuration of all the mechanism components. The representations of the mechanism for situations A to E (Fig.3a) are given in Fig.3c. Square symbols in Fig.3a indicate values of θ_{1i} and θ_{2i}, $i \in \{1, 2, 3\}$ that belong to the same septuplet. Arrows indicate how the joint values vary with λ for this situation.

For this situation, analytical relationships between the end-effector position and the joint values can be established after a specific analytical derivation, as detailed in Appendix B. The corresponding representation of the bifurcation diagram is presented in Fig. 3b for sake of comparison. The accuracy of the continuation-based analysis is confirmed: Fig. 3b corresponds to Fig. 3a after inclusion of the symmetry with respect to $z_G = 0$.

A bifurcation point is identified when the end-effector is in the base plane, which happens for the two situations $(\theta_{1i}, \theta_{2i}) = (0, 0)$ and $(\theta_{1i}, \theta_{2i}) = (\pi, 0)$, $i \in \{1, 2, 3\}$. They are indicated by red circles in Fig.3a. When leaving the configuration A or E (Fig.3c) to reach non-planar configurations, it is possible to get two distinct pairs of values of θ_{1i} and θ_{2i}, $i \in \{1, 2, 3\}$ for one pose of the end-effector. This indicates the presence of two configurations for the legs for a single end-effector pose. This can be observed in situations B, C and D in Fig. 3c where the legs 1 and 2 are in one configuration and the leg 3 is in the other configuration. The branches describing the two different leg configurations do not exhibit same shape, nor the same slope at the origin $z_G = 0$. In other words, the V-profile of the curves representing the evolution of θ_{2i}, $i \in \{1, 2, 3\}$, differs from the variation of θ_{1i}, $i \in \{1, 2, 3\}$. One can see here that the proposed evaluation method allows the designer to easily apprehend such differences, without any linearization of the mechanism kinematics for local analysis as usually performed. It can be for instance beneficial to choose as active joints the ones with lowest slopes at the origin since the actuator ranges of motion will be lowered for a given end-effector displacement.

When the joints θ_{1i}, $i \in \{1, 2, 3\}$ are actuated, we observe at points A and E that the curves $\theta_{1i}(z_G)$ present a vertical tangent: the platform can move locally without any variation of θ_{1i}, $i \in \{1, 2, 3\}$. This signifies that the mechanism undergoes a parallel singularity, which is in accordance with the results obtained in a previous work [14]. This means that we can visualize the presence of a parallel singularity from the bifurcation diagram. The detection is possible if the path used to build the diagram corresponds to the instantaneous motion gained by the mechanism end-effector, which is here the case with an out-of-plane translation [14]. Singular configurations are interesting as they can be candidate configurations for singularity-based compliant mechanism design as the one developed in [12]. In addition, in the vicinity of such a singular configuration, a high amplification ratio can be obtained for θ_{1i} when the branches of solutions are those presenting vertical tangents. This is of particular interest when piezoelectric actuators requiring mechanical amplification are needed, as it is the case in many compliant mechanical amplifiers.

When the end-effector is at the maximum height (configuration C in Fig. 3a and Fig. 3b), a so-called turning point is reached, *i.e.* an extreme point. The absence of infinitesimal displacement δz_G about that configuration implies that the end-effector does not exhibit any translational motion. No end-effector displacement is obtained while the variables describing the leg joints vary. Within the same exploration we here identify a serial singularity corresponding to a workspace limit. Such situation can also be employed for a compliant mechanism as in its vicinity it can be used as a way to increase the mechanism resolution.

4.3. Multiple bifurcations, architectural singularity and self-motion

The bifurcation diagram presented in Fig 4a plots the branches of solutions when the centroid G is driven along a circle of radius R at height $z_G = R$, that is by considering the path $(\rho_G, \phi_G, z_G) = (10, \lambda, 10)$.

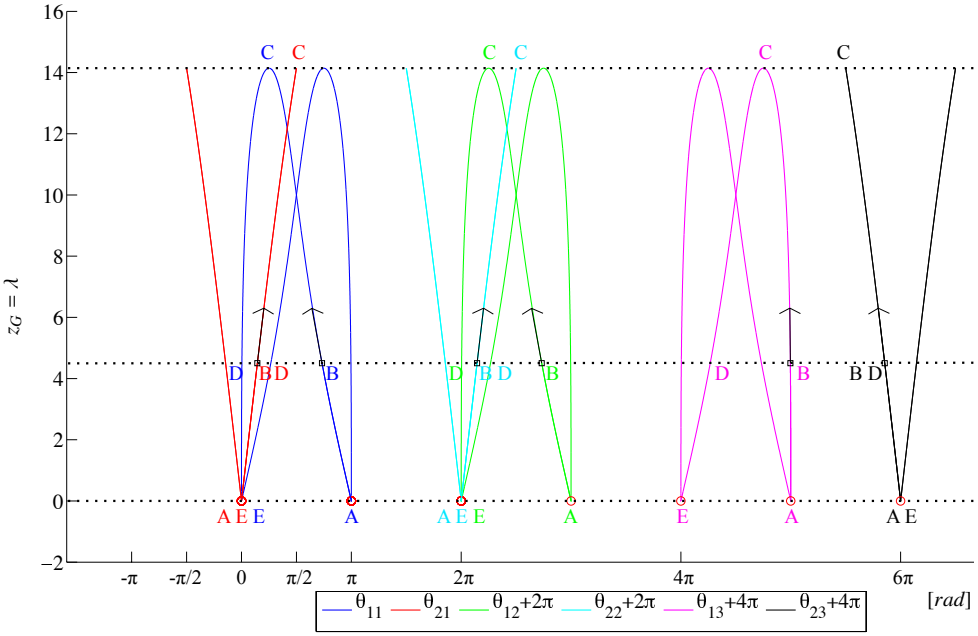

(a) Bifurcation diagram.

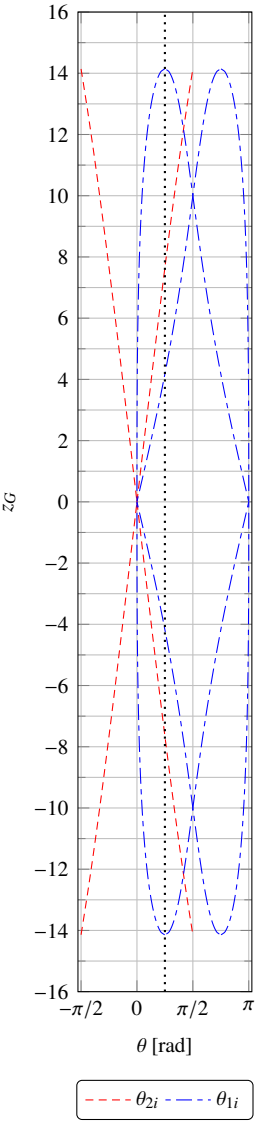

(b) Analytical results (Appendix B).

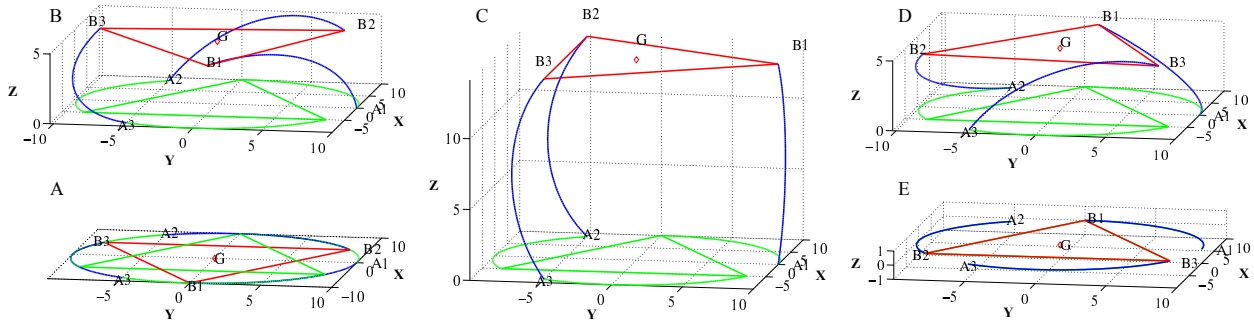

(c) Poses at labelled points A to E. The planar configuration with null joint angles is plotted in green.

Figure 3: Numerical and analytical bifurcation diagrams, with associated mechanism configurations, for $(\phi_G, \rho_G) = (0, 0)$.

The diagram is composed of two curves for each of the six components (θ_{11}, θ_{21}, θ_{12}, θ_{22}, θ_{13}, θ_{23}) that are part of the state vector $\mathbf{u}$. In Fig.4a, the plots of $(\theta_{12}, \theta_{22})$ and $(\theta_{13}, \theta_{23})$ are again shifted for the sake of clarity. For each joint variable, it is possible to switch between two paths at bifurcation points represented by red circles. The bifurcations do not occur for a single value of the angle ϕ_G but with $2\pi/3$ shifts: six bifurcations are detected along the end-effector path.

One solution branch corresponds to $\theta_{1i} = \pi/2$, $i \in \{1, 2, 3\}$ (vertical curves on Fig.4a) with simultaneous linear variation of the angles θ_{2i}, $i \in \{1, 2, 3\}$. As outlined by Fig.4b, the end-effector exhibits a circular movement such that $(O, \mathbf{z})$ remains normal to the end-effector plane. Since the first joint angles are constant, it means the end-effector can move in this situation even if the first joints on the base are maintained in their initial position. We can here observe the existence of an architectural singularity [48], also called a self-motion. The continuation method allows us to observe this particular motion using only the closed-loop equations. In addition, we can see that it is also possible for the end-effector to describe a motion of circular shape without being permanently in singularity (see configurations E-F on Fig.4b).

The three different joint evolutions observed during the platform motion have basically constant, linear or sinusoidal shapes. Once again, the bifurcation diagram gives the designer immediate and precise information on the joint angle evolutions so he can pick-up the most suitable configurations of the mechanism for the design of a compliant mechanism. Here, it is possible to obtain end-effector displacement with no velocity of θ_{1i}. This means the joints θ_{1i} could be removed and thus the compliant mechanism architecture could be greatly simplified without modification of the desired end-effector motion. At the same time, linear or sinusoidal evolutions of the other joint angles can be exploited. The designer can make his decision depending on the most suitable input-output relationship for the application. In particular, there is a factor two in the total range of motion on the joints (see Fig. 4a) between the two situations for one gyration of the platform, which may be a determinant indicator.

Finally, one can observe that the bifurcation points allow the legs to switch from one profile to the other, for example from a sinusoidal profile to a constant profile when considering the evolution of θ_{1i}. If the joints θ_{1i} are actuated and the mechanism passes through a bifurcation point, there is a chance to lose control of the platform. In this situation, the bifurcation points are probably configurations to be avoided by the designer.

4.4. Workspace estimation

The reachable workspace is the set of all positions that can be reached by the point G for at least one orientation of the mobile platform. The shape of the workspace can help the designer to choose a design configuration regarding the integration constraints. It is here obtained by extracting the local and global boundaries for each bifurcation diagram obtained for a discrete map of positions (ϕ_G, ρ_G) with a continuous exploration of z_G. We therefore obtain a semi-discrete volume approximating the maximal workspace.

Workspace estimation can be simplified by taking into account mechanism symmetries. The mechanism is invariant with respect to a rotation of $\frac{2\pi}{3}$ radians around the axis $(O, \mathbf{z})$. The workspace of each leg end is also symmetric with respect to the plane $(O, \mathbf{OA_i}, \mathbf{z})$ (Fig. 1). As said before, the $(O, \mathbf{x}, \mathbf{y})$ plane is a symmetry plane for the mechanism. The workspace can thus be computed from one twelfth defined by $0 \leq \phi_G \leq \frac{\pi}{3}$ and $z_G \geq 0$ and completed by circular pattern repetition and symmetry.

In order to efficiently build the semi-discrete volume, an adaptive technique inspired from [50] is adopted. It is based on a Newton-Raphson (NR) method to find an initial approximation at a given (ϕ_G, ρ_G). Then we associate Diamanlab for the computation of branches of solutions along the path $\lambda = z_G$ to an iterative management of the 2D grid construction. This construction encloses an angular *do loop* in the range $[0, \frac{\pi}{3}]$ with a step of $\pi/90$ radians (2°), and an adaptive loop performed on the radii ρ. This runs from $\rho = 1$ to $\rho = L$ with a step of $\delta\rho = 1$. The checkpoints computed for the current (ϕ_G, ρ_G) are used as initial guesses for the NR method (until the NR convergence). If the NR method fails, the step $\delta\rho$ is divided by two and the NR method is run again. The loop on ρ stops when $\delta\rho < 0.01$. This allows the building of the upper part of Fig.5. The lower part is built using the same process for $\phi_G \in [0, \frac{\pi}{3}]$ and ρ_G running from 10 down to 0. The lower checkpoints of the solution branches computed for $\rho_G = 10$ are used as initial approximations. The surfaces that delimit the reachable workspace[2] are represented in Fig.6.

[2] 3D figures are provided as supplementary material.

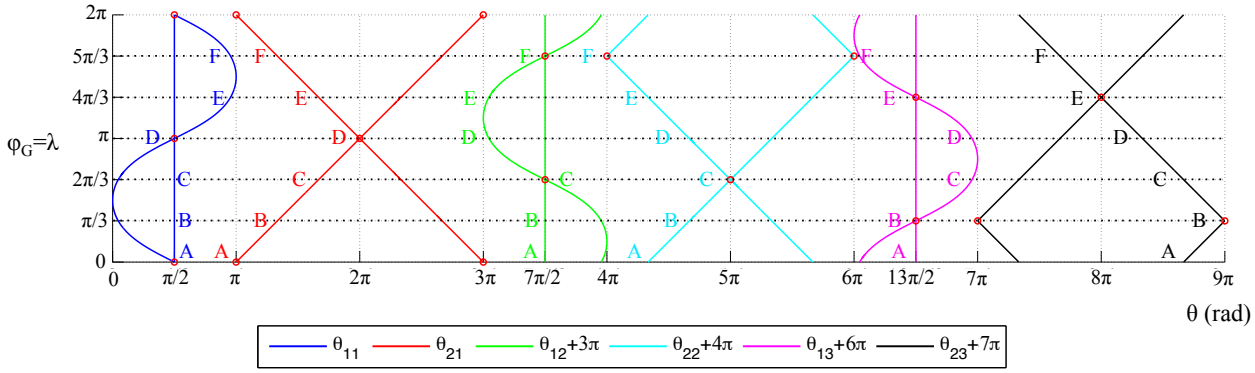

(a) Bifurcation diagram with labelled points.

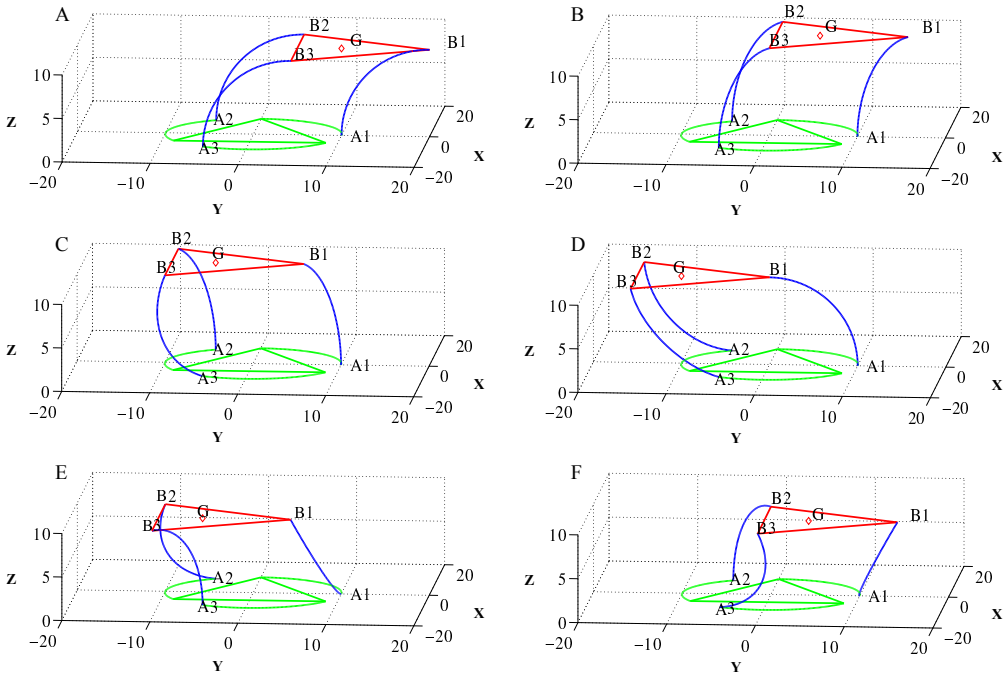

(b) Poses at labelled points. The planar configuration with null joint angles is plotted in green.

Figure 4: Bifurcation diagram and associated mechanism configurations for $(\rho_G, z_G) = (10, 10)$.

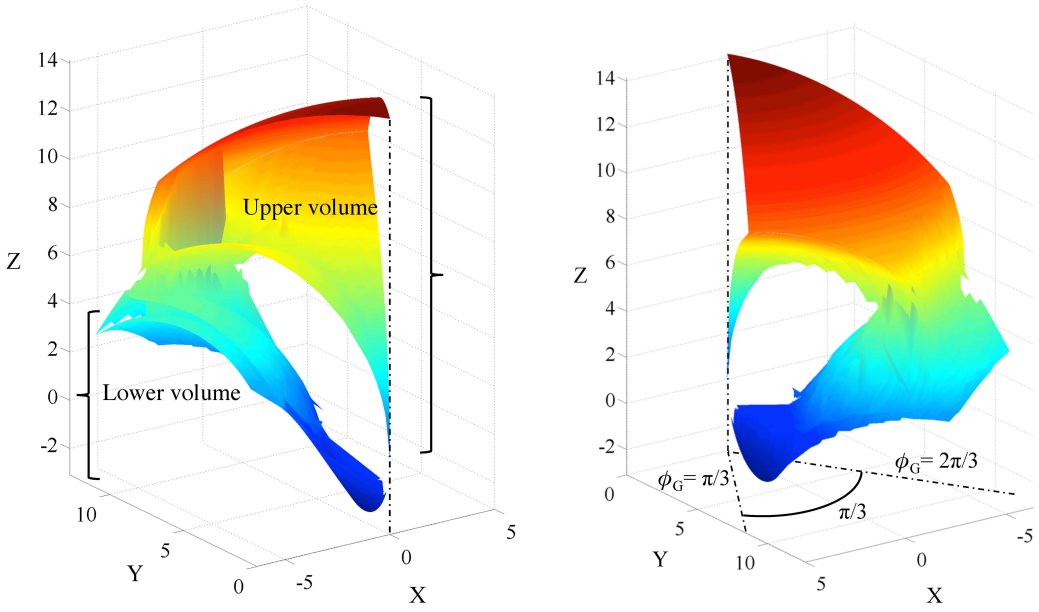

(a) Front view. (b) Back view.

Figure 5: 3D views of 1/12th of the reachable workspace ($\alpha = \pi/2$; $R = 10$; $\phi_G \in [\pi/3; 2\pi/3]$).

The reachable workspace is mainly composed of two parts, which can be seen on Fig.5a as upper and lower volumes. The upper volume can be described as the volume existing between a portion of the sphere of radius L (superimposed on Fig. 6) for $z_G \in [L_1; L] = [10; 10\sqrt{2}]$ and a surface that is going through the center O. The funnel shape along the vertical z-axis indicate restricted displacement along x- and y-axis which can help the designer to make a decision of considering or not this workspace area. The lower volume is a set of end-effector positions that can be reached with flipped configurations, *a priori* complex to integrate and probably of lesser interest for the designer. Further analysis shows that this lower volume exists only for $\alpha \in [\pi/3, \pi/3 + \pi]$. If α is not in this interval, only the upper volume remains.

The shape of the workspace gives the designer the available volume and in addition it indicates the existence of workspace areas that are close but non-connected through a direct end-effector path. Once again, such information on the mechanism has been obtained using only basic knowledge on the mechanism, namely the closed-loop equations.

5. Conclusions and outlook

This paper presents the use of higher-order continuation method for the preliminary design of compliant mechanisms using the rigid-body replacement method. The method is general. It can be applied to any mechanism since only the geometrical closed-loop equations are required. It results in continuous bifurcation diagrams revealing the kinematic input-output relationships as well as the presence of parallel singularities, serial singularities, architectural singularities and workspace boundaries. The advantage of the method is fourfold:

1. The bifurcation diagrams give the input-output coordinate relationships for a given end-effector path. This is helpful in selecting the most appropriate mechanism working configuration.
2. The different possible joint velocity profiles for a given end-effector path are made visible. This is helpful in selecting the joints to be actuated. Those with non-linear behavior can be interesting for particular actuators such as piezoelectric actuators requiring mechanical amplification.
3. Singular configurations are identified which may be considered as candidates for singularity-based compliant mechanism design [12]. Some of the ones identified for the 3–US mechanism have never been described in the literature, to our best knowledge.

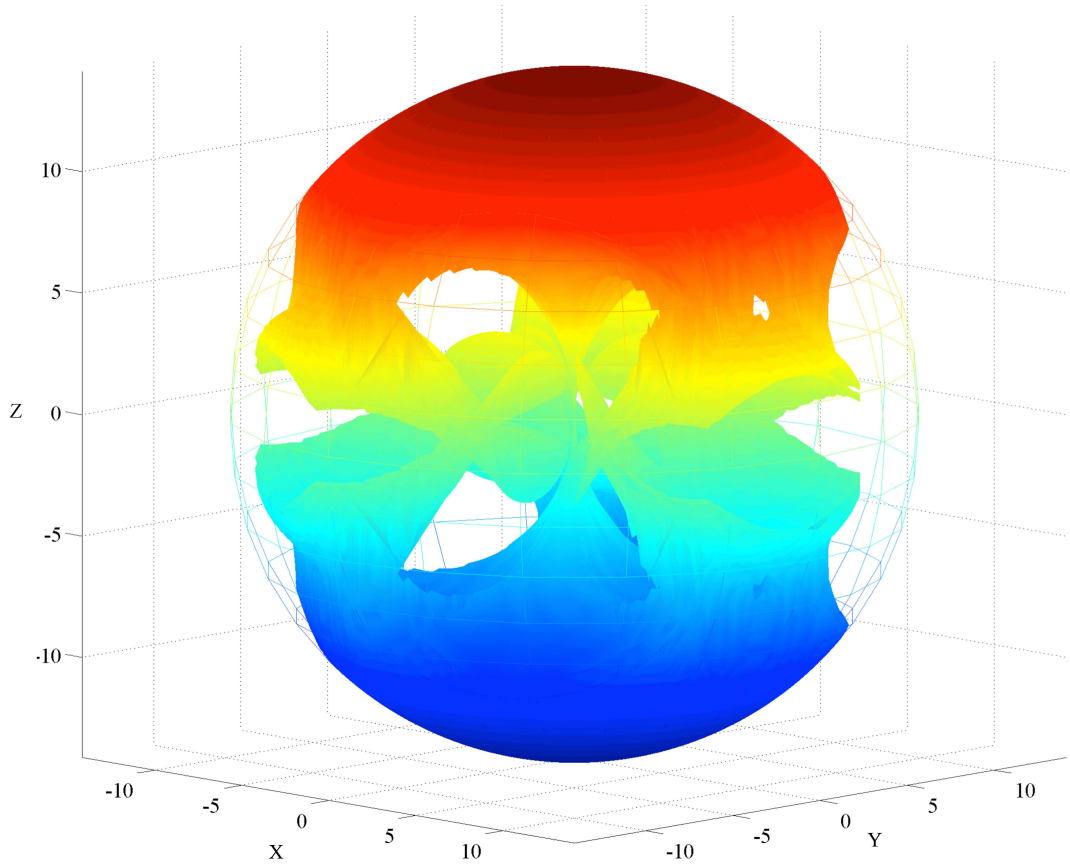

Figure 6: 3D view of the reachable workspace ($\alpha = \pi/2$; $R = 10$).

4. The workspace boundary defines the exact volume within which the end-effector can move. The possible presence of disconnected portions of the workspace which, despite mutual proximity, are not be connected by admissible trajectories is detected.

A 3–US mechanism has been analyzed in order to illustrate the relevance of the method for the design of compliant mechanisms. The proposed analysis clearly shows the mechanism's properties and interests: a large reachable workspace and particular kinematic behavior as screw motion and platform gyration. These latter are respectively illustrated with their bifurcation diagrams and commented.

Future works are to consider sensitivity analysis, already provided by Diamant [51, 52], to give the designer additional information on, for instance, the sensitivity of kinematic properties to manufacturing errors. This point is currently under investigation.

Appendix A. Diamanlab implementation for the 3–US residual equations

```
function Residual= R(obj,U)
global Ck
%Input geometrical data
 R=10;       %mechanism radius
 alpha=90*pi/180; %angle AiOBi expressed in radius
 xw=0; yw=0;    %fixed abcissa and ordinate for the centroid X of the platform
%The Diamanlab unknown U=(X,zw) is split as follows
 zw=U(7);      %Height of the centroid X of the platform, continuation parameter
 X(1:6)=U(1:6);  %output coordinates X
if isa(U,'Taylor')
  Residual=Taylor(get(U,'order'),zeros(get(obj,'neq'),1));
else
  Residual=zeros(get(obj,'neq'),1);
end
%Local geometrical parameters
 L=2*R*sin(alpha/2);             %leg chord
 alpha1=alpha; alpha2=alpha; alpha3=alpha; %angles AiOBi (all equal, here)
%projection of the ith cord on the x- and y_axis, respectively
 L1x=R*sin(alpha1); L1y=2*R*(sin(alpha1/2))^2; %independent from zw
 L2x=R*sin(alpha2); L2y=2*R*(sin(alpha2/2))^2;
 L3x=R*sin(alpha3); L3y=2*R*(sin(alpha3/2))^2;
%Equation (2): Coordinates of B1
 xB1=R-L1y*cos(X(2));
 yB1=(L1x*cos(X(1))-L1y*sin(X(2))*sin(X(1)));
 zB1=L1x*sin(X(1))+L1y*sin(X(2))*cos(X(1));
%Equation (2): Coordinates of B2
 xB2=(R-L2y*cos(X(4)))*cos(2*pi/3)-(L2x*cos(X(3))-L1y*sin(X(4))*sin(X(3)))*sin(2*pi/3);
 yB2=(L2x*cos(X(3))-L2y*sin(X(4))*sin(X(3)))*cos(2*pi/3)+(R-L2y*cos(X(4)))*sin(2*pi/3);
 zB2=L2x*sin(X(3))+L2y*sin(X(4))*cos(X(3));
%Equation (2): Coordinates of B3
 xB3=(R-L3y*cos(X(6)))*cos(4*pi/3)-(L3x*cos(X(5))-L3y*sin(X(6))*sin(X(5)))*sin(4*pi/3);
 yB3=(L3x*cos(X(5))-L3y*sin(X(6))*sin(X(5)))*cos(4*pi/3)+(R-L3y*cos(X(6)))*sin(4*pi/3);
 zB3=L3x*sin(X(5))+L3y*sin(X(6))*cos(X(5));
%Distances between the spherical joint centers
 d12=sqrt((xB1-xB2)^2+(yB1-yB2)^2+(zB1-zB2)^2); %||B1B2||
 d23=sqrt((xB3-xB2)^2+(yB3-yB2)^2+(zB3-zB2)^2); %||B1B2||
 d13=sqrt((xB3-xB1)^2+(yB3-yB1)^2+(zB3-zB1)^2); %||B1B3||
%Equation (1)
%Coordinates of the centroid G of the triangle B1B2B3
 xG=(xB1+xB2+xB3)/3; yG=(yB1+yB2+yB3)/3; zG=(zB1+zB2+zB3)/3;
%Calculation of the 6 components of the residual
%Constraint (3): ||B1B2||=||B2B3||=||B1B3||=sqrt(3)*R
 Residual(1)=d12-sqrt(3)*R; Residual(2)=d23-sqrt(3)*R; Residual(3)=d13-sqrt(3)*R;
%Constraint imposing G=X
 Residual(4)=xG-xw;     Residual(5)=yG-yw;     Residual(6)=zG-zw;
end
```

Appendix B. Analytical computation of the bifurcation diagram related to the screw motion

Parameterization

The three legs behave identically during the mechanism screw motion. Only the first leg is therefore considered and we will not designate in the following the leg number by a subscript index. The cartesian coordinates of point B as a function of the angles

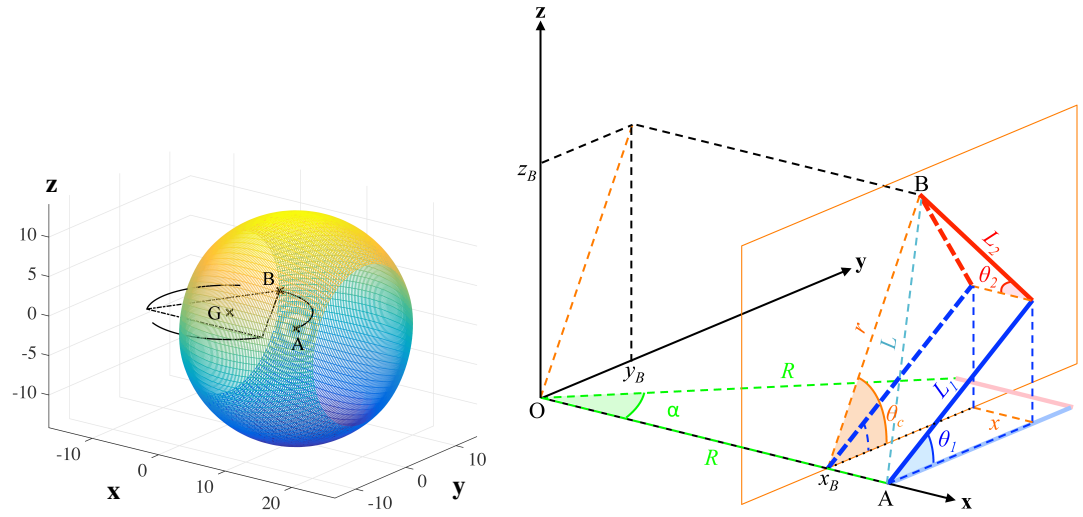

(a) Maximal workspace of a leg for $R = 10$ and $\alpha = \pi/2$.

(b) Cylindrical coordinates of B.

Figure B.7: Parameterization of the leg end B and its workspace.

θ_1 and θ_2 (Fig. B.7b) are equal to:

$$\mathbf{OB} = \begin{pmatrix} R - L_2\cos(\theta_2) \\ L_1\cos(\theta_1) - L_2\sin(\theta_2)\sin(\theta_1) \\ L_1\sin(\theta_1) + L_2\sin(\theta_2)\cos(\theta_1) \end{pmatrix}, \tag{B.1}$$

with $L_1 = R\sin(\alpha)$ and $L_2 = 2R\sin(\alpha/2)^2$. If disconnected from the platform, the tip of the leg B can describe a truncated sphere of radius $2R\sin\left(\frac{\alpha}{2}\right)$ around the axis of its first revolute joint (Figure B.7a). Cylindrical coordinates (r, θ_c, x) are used with the revolute joint axis $(O, \mathbf{x})$ defined as the cylindrical axis (Fig. B.7b). The cartesian coordinates of point B are thus also equal to:

$$\mathbf{OB} = \begin{pmatrix} R + x \\ r\cos(\theta_c) \\ r\sin(\theta_c) \end{pmatrix} = \begin{pmatrix} R + x \\ \sqrt{L^2 - x^2}\cos(\theta_c) \\ \sqrt{L^2 - x^2}\sin(\theta_c) \end{pmatrix}, \tag{B.2}$$

with $x = -L_2\cos(\theta_2)$ and $L = 2R\sin(\alpha/2)$.

The altitude of the platform z_G is equal to the third component of $\mathbf{OB}$. Building analytically the bifurcation diagram requires the derivation of the relationships between the angles θ_1, θ_2 and z_G.

Analytical relationship between the altitude z_G and the angle θ_2

During the platform motion, the point B remains at a distance R from $(O, \mathbf{z})$. The projection of B on the plane $(O, \mathbf{x}, \mathbf{y})$ lies therefore on a circle of radius R and the relation between θ_c and x is:

$$R^2 = (R + x)^2 + \left(\sqrt{L^2 - x^2}\cos(\theta_c)\right)^2. \tag{B.3}$$

Expressing θ_c in terms of x, yields the four solutions:

$$\theta_c \in \left\{ \pm\arccos\left(\sqrt{\frac{x^2 + 2R\cdot x}{x^2 - L^2}}\right), \pi \pm \arccos\left(\sqrt{\frac{x^2 + 2R\cdot x}{x^2 - L^2}}\right) \right\}. \tag{B.4}$$

with $x \neq \pm L$ which is guaranteed since $x = -L_2\cos(\theta_2)$ from (B.1) gives $x \in [-L_2, L_2]$ and $L_2 < L$. Using the relation $x = -L_2\cos(\theta_2)$ in (B.4) gives:

$$z_G = \sqrt{L^2 - x^2}\sin\left(\pm\arccos\left(\sqrt{\frac{x^2 + 2R\cdot x}{x^2 - L^2}}\right)\right) = \pm L\sqrt{1 - \cos(\theta_2)} \tag{B.5}$$

which gives the analytical relation between z_G and θ_2.

The derivative of z_G with respect to θ_2 is not defined for $\theta_2 = 0$, but a power series in $\theta_2 = 0$ indicates that:

$$\begin{cases} \lim\limits_{\theta_2 \to 0^-} \dfrac{dz_G}{d\theta_2} = -\dfrac{L}{\sqrt{2}}, \\ \lim\limits_{\theta_2 \to 0^+} \dfrac{dz_G}{d\theta_2} = \dfrac{L}{\sqrt{2}}. \end{cases} . \tag{B.6}$$

with $L = 2R\sin\left(\frac{\alpha}{2}\right)$. This confirms the tangent discontinuity observed on the analytical bifurcation diagram of Fig. 3b.

Analytical relationship between the altitude z_G and the angle θ_1

The angle θ_2 can be expressed as a function of z_G from equation (B.5):

$$\theta_2 = \arccos\left(1 - \frac{z_G^2}{L^2}\right), \tag{B.7}$$

with $L = 2R\sin\left(\frac{\alpha}{2}\right)$. Using (B.7) in (B.1), one deduces:

$$z_G = L_1\sin(\theta_1) + L_2\sin\left(\arccos\left(1 - \frac{z_G^2}{L^2}\right)\right)\cos(\theta_1) = L_1\sin(\theta_1) + L_2\sqrt{1 - \left(1 - \frac{z_G^2}{L^2}\right)^2}\cos(\theta_1). \tag{B.8}$$

Four values of θ_1 can be obtained as functions of z_G:

$$\theta_1 \in \left\{ 2\arctan\left(\frac{L_1 \pm \sqrt{c(z_G)^2 + L_1^2 - z_G^2}}{c(z_G) + z_G}\right), \pi - 2\arctan\left(\frac{L_1 \pm \sqrt{c(z_G)^2 + L_1^2 - z_G^2}}{c(z_G) + z_G}\right) \right\} \tag{B.9}$$

for $z_G \neq \pm\frac{L\sqrt{2L_2^2 - L^2}}{L_2}$ with $c(z_G) = L_2\sqrt{1 - \left(1 - \frac{z_G^2}{L^2}\right)^2}$, $L_1 = R\sin(\alpha)$, $L_2 = 2R\sin(\alpha/2)^2$. This allows us to build the second part of the bifurcation diagram in Fig. 3b

References

[1] L.L. Howell, Compliant Mechanisms, Wiley, 2001.

[2] L.L. Howell and Spencer P. Magleby and Brian M. Olsen, Handbook of Compliant Mechanisms, Wiley, 2013.

[3] Y. Tian, B. Shirinzadeh and D. Zhang, Design and dynamics of a 3-DOF flexure-based parallel mechanism for micro/nano manipulation, Journal of Microelectronic Engineering, 2010, 230–241.

[4] S. Awtar and Alexander H. Slocum , Constraint-Based Design of Parallel Kinematic XY Flexure Mechanisms, 2006, Journal of Mechanical Design 129(8), 816–830.

[5] L. Rubbert, P. Renaud and J. Gangloff, Design and Optimization for a Cardiac Stabilizer Based on Planar Parallel Compliant Mechanisms, ASME ESDA, 2012, Nantes, France, Paper No. ESDA2012-82278, pp. 235-244.

[6] W. Bachta, P. Renaud, E. Laroche and J. Gangloff, The Cardiolock Project: Design of an Active Cardiac Stabilizer for Cardiac Surgery, ASME Journal of Mechanical Design, Vol. 133, n7, pp. 071002-1–071002-10, July 2011.

[7] Y. Fang, L.-W. Tsai, Structure synthesis of a class of 4-DOF and 5-DOF parallel manipulators with identical limb structures, Int. J. Robot. Res. 21 (2002) 799–810.

[8] J.-P. Merlet, Parallel robots, Springer, 2006.

[9] S. Briot, V. Arakelian, I. A. Bonev, D. Chablat P. Wenger, Self-Motions of General 3-RPR Planar Parallel Robots ,The International Journal of Robotics Research, Vol 27, Issue 7, pp. 855-866, 2008.

[10] W. Khalil and O. Ibrahim, General solution for the dynamic modeling of parallel robots, in proceedings of IEEE International Conference on Robotics and Automation, pp. 3665-3670 Vol.4, 2004.

[11] A. Yu, I. A. Bonev, P. Zsombor-Murray, Geometric approach to the accuracy analysis of a class of 3-DOF planar parallel robots, Mechanism and Machine Theory, Volume 43, Issue 3, March 2008, Pages 364-375, ISSN 0094-114X.

[12] L. Rubbert, S. Caro, J. Gangloff, P. Renaud, Using singularities of parallel manipulators to enhance the rigid-body replacement design method of compliant mechanisms, J. Mech. Design 136 (2014) 051010.

[13] Y. Qin, J. S. Dai, Forward displacement analysis of two foldable 3-US parallel mechanisms, in: J. S. Dai, M. Zoppi, X. Kong (Eds.), Advances in Reconfigurable Mechanisms and Robots I, Springer London, 2012, pp. 805–814.

[14] L. Rubbert, S. Caro, P. Renaud, J. Gangloff, A planar RRP compliant mechanism based on the singularity analysis of a 3-US parallel mechanism, in: J. Lenarcic, M. Husty (Eds.), Advances in Robot Kinematics, Springer Netherlands, 2012, pp. 381–388.

[15] J. Rasetgar, D. Perel, Generation of manipulator workspace boundary geometry using the monte carlo method and interactive computer graphics, J. Mech. Design 112 (1990) 452–454.

[16] O. Bohigas, M. Manubens, L. Ros, A complete method for workspace boundary determination on general structure manipulators, IEEE Trans. Robot. 28 (2012) 993–1006.

[17] S. Ahmad, S. Luo, Analysis of kinematic singularities for robot manipulators in Cartesian coordinate parameters, in: Proceedings of the IEEE International Conference on Robotics and Automation, 1988, pp. 840–845.
[18] Z.C. Lai, D.C.H. Yang, A new method for the singularity analysis of simple six-link manipulators, Int. J. Robot. Res. 5 (1986) 66–74.
[19] F. Litvin, Application of theorem of implicit function system existence for analysis and synthesis of linkages, Mech. Mach. Theory 15 (1980) 115–125.
[20] E. Haug, C.-M. Luh, F. Adkins, J.-Y. Wang, Numerical algorithms for mapping boundaries of manipulator workspaces, J. Mech. Des. 118 (1996) 228–234.
[21] G. Hentz, I. Charpentier, P. Renaud, Higher-order continuation for the determination of robot workspace boundaries, C. R. Mecanique 344 (2016) 95–101.
[22] Q. Boehler, I. Charpentier, M. Vedrines, P. Renaud. Definition and Computation of Tensegrity Mechanism Workspace, ASME Journal of Mechanisms and Robotics 7 (2016) 044502
[23] I. Charpentier, M. Potier-Ferry, Différentiation automatique de la méthode asymptotique numérique typée: l'approche Diamant, C. R. Mecanique 336 (2008) 336–340.
[24] I. Charpentier, On higher-order differentiation in nonlinear mechanics, Optim. Method. Softw. 27 (2012) 221–232.
[25] I. Charpentier, B. Cochelin, K. Lampoh, Diamanlab - an interactive taylor-based continuation tool in matlab, HAL 0085359,
[26] W. Govaerts, Y. Kuznetzov, Interactive continuation tools, in: B. Krauskopf et al. (Eds.), Numerical Continuation Methods for Dynamical Systems, Springer Netherlands, 2007, pp. 51–75.
[27] H. Keller, Lectures on numerical methods in bifurcation problems, Springer-Verlag, Berlin, 1987.
[28] E.L. Allgower, K. Georg, Numerical Continuation Methods: an Introduction, Springer-Verlag, New-York, 1990.
[29] E. Doedel, H. Keller, J. Kernevez, Numerical analysis and control of bifurcation problems (i) bifurcation in finite dimensions, Int. J. Bifurcat. Chaos 1 (1991) 493–520.
[30] R. Seydel, Practical Bifurcation and Stability Analysis, no. 5 in Interdisciplinary Applied Mathematics, Springer, 2009.
[31] Y. Chang, G. F. Corliss, Solving ordinary differential equations using Taylor series, ACM T. Math. Software 8 (1982) 114–144.
[32] P. Guillaume, M. Masmoudi, Computation of high order derivatives in optimal shape design, Numer. Math. 67 (1994) 231–250.
[33] M. Berz, K. Makino, K. Shamseddine, G. Hoffstätter, W. Wan, COSY INFINITY and its applications in nonlinear dynamics, in: M. Berz, C. Bischof, G. Corliss, A. Griewank (Eds.), Computational Differentiation: Techniques, Applications, and Tools, SIAM, Philadelphia, 1996, pp. 363–365.
[34] N. Nedialkov, J. Pryce, Solving differential-algebraic equations by Taylor series (I): Computing Taylor coefficients, BIT 45 (2005) 561–591.
[35] A. Griewank, D. Juedes, J. Utke, ADOL–C, a package for the automatic differentiation of algorithms written in C/C++, ACM T. Math. Software 22 (2) (1996) 131–167.
[36] I. Charpentier, J. Utke, Fast higher-order derivative tensors with Rapsodia, Optim. Method. Softw. 24 (2009) 1–14.
[37] J. Thompson, A. Walker, The nonlinear perturbation analysis of discrete structural systems, Int. J. Solids Struct. 4 (1968) 757–768.
[38] B. Cochelin, N. Damil, M. Potier-Ferry, Méthode asymptotique numérique, Hermes Science Publications, Paris, 2007.
[39] M. Bilasse, I. Charpentier, E. Daya, Y. Koutsawa, A generic approach for the solution of nonlinear residual equations. Part II: Homotopy and complex nonlinear eigenvalue method, Comput. Method. Appl. M. 198 (2009) 3999–4004.
[40] B. Cochelin, M. Médale, Power series analysis as a major breakthrough to improve the efficiency of asymptotic numerical method in the vicinity of bifurcations, J. Comput. Phys. 236 (2013) 594–607.
[41] Y. Guevel, H. Boutyour, J.M. Cadou, Automatic detection and branch switching methods for steady bifurcation in fluid mechanics, J. Comput. Phys. 230 (2011) 3614–3629.
[42] I. Charpentier, B. Cochelin, K. Lampoh, Diamanlab v1.0: An interactive Taylor-based continuation tool in MATLAB, Software protected by Agence de Protection des Programmes, 2014. IDDN.FR.001.440012.S.P.000.2014.000.31235. Downloadable from http://icube-web.unistra.fr/cs/index.php/Fichier:Diamanlab.zip
[43] A. Griewank, A. Walther, Algorithm 799: Revolve: An implementation of checkpoint for the reverse or adjoint mode of computational differentiation, ACM T. Math. Software 26 (2000) 19–45.
[44] I. Charpentier, Checkpointing schemes of adjoint codes: Application to the meteorological model Meso-NH, SIAM J. Sci. Comput. 22 (2001) 2135–2151.
[45] R. Vertechy, V. Parenti-Castelli, Static and stiffness analyses of a class of over-constrained parallel manipulators with legs of type us and ups, in: Proceedings of the IEEE International Conference on Robotics and Automation, 2007, pp. 561–567.
[46] C. Andersen, S. Magleby, L. Howell, Principles and preliminary concepts for compliant mechanically reactive armor, in: ASME/IFToMM International Conference on Reconfigurable Mechanisms and Robots, 2009, pp. 370–376.
[47] D. Chablat, P. Wenger, Working modes and aspects in fully parallel manipulator, in: Proceedings of the IEEE International Conference on Robotics and Automation, 1998, pp. 1970–1976.
[48] O. Ma, J. Angeles, Architecture singularities of platform manipulators, in: Proceedings of the IEEE International Conference ohigher-ordern Robotics and Automation, 1991, pp. 1542–1547.
[49] I. Bonev, D. Zlatanov, C. M. Gosselin, Singularity analysis of 3-DOF planar parallel mechanisms via screw theory, J. Mech. Design 125 (2003) 573–581.
[50] I. Charpentier, N. Jakse, Exact derivatives of the pair-correlation function of simple liquids using the linear tangent method: application to self-consistent integral equations, J. Chem. Phys. 114 (2001) 2284–2292.
[51] I. Charpentier Sensitivity of solutions computed through the asymptotic numerical method. Comptes Rendus Mecanique 336 (2008) 788-793.
[52] I. Charpentier, K. Lampoh, Sensitivity computations in higher order continuation methods, Applied Mathematical Modelling, 40 (2016) 3365–3380.